The origin of *SH*-wave resonance frequencies in sedimentary layers

Mirko van der Baan*

Department of Physics, University of Alberta, Edmonton, Alberta, T6G 2G7 *Canada. E-mail: mirko.vanderbaan@ualberta.ca*

SUMMARY
Resonance frequencies are often analysed in geo-engineering studies to evaluate seismic risk and microzonation in urban areas. The Nakamura technique constitutes a popular approach that computes the spectral ratio of horizontal-to-vertical ground motion in ambient noise recordings to reveal the existence of any site resonance frequencies. Its theoretical basis remains however unclear with some authors arguing that the method de-emphasizes any Rayleigh-wave contributions and that the resonance frequencies are solely caused by vertically incident *SH* waves. Other authors explain the same resonance frequencies by the ellipticity of the fundamental Rayleigh wave. Recent numerical simulations reveal that the magnitude of the peak frequency is proportional to the relative portion of Love waves present.

This study demonstrates that Love waves alone can be responsible for any observed resonance frequencies in sedimentary layers. Yet sharp *SH*-wave resonance frequencies are only excited by a source in the bedrock.

These resonance frequencies are caused by inhomogeneous waves excited by the bedrock source that tunnel through the high-velocity bedrock to emerge in the low-velocity sediments with a very reduced range of slownesses. The resulting *SH* waves are then free to interfere constructively thereby creating the observed resonance frequencies. This general trigger mechanism leads to resonances that are almost offset independent.

The resulting resonance frequencies map onto points of maximum curvature in the Love-wave phase–velocity dispersion curves at or just beyond the critical horizontal slowness. They can be analysed with the quarter-wavelength law if a large velocity contrast exists between the unconsolidated sediments and the bedrock. A minor modification of the quarter-wavelength law provides more accurate predictions, also for smaller velocity contrasts.

Multisource simulations show that site amplification factors as determined by horizontal-over-vertical (H/V) spectral ratios would not only depend on the relative portion of Love waves in the total wavefield but also on the depth distribution and the relative strength of the *SH* sources inside the bedrock compared with those in the sediments. An accurate interpretation of site amplification factors by means of H/V peak frequencies would thus require in-depth knowledge of the causes and origins of the local microseismic noise field.

Key words: Time series analysis; Fourier analysis; Earthquake ground motions; Guided waves; Site effects; Wave propagation.

1 INTRODUCTION

Site amplification studies constitute an important tool to assess seismic risk and microzonation in urban areas since regional variations in ground shaking must be accounted for in national building and construction norms. Site amplification is generally related to the presence and thickness of soft sedimentary layers (Borcherdt 1970; Nakamura 1989; Lermo & Chávez-García 1994; Field & Jacob 1995). A rich literature exists therefore detailing studies on

local variations in resonance frequencies and amplification factors (Bonnefoy-Claudet *et al.* 2006b).

One of the most popular and cost-effective approaches to determine the thickness of any sedimentary layers consists of the analysis of ambient noise characteristics using the microtremor survey technique of Nogoshi & Igarashi (1971) as revised by Nakamura (1989). This technique measures the spectral ratio of horizontal-over-vertical (H/V) ground motion in ambient noise recordings providing reliable information on resonance frequencies (Field & Jacob 1993, 1995; Lermo & Chávez-García 1994; Bonnefoy-Claudet *et al.* 2006b) and possibly even site amplification factors. However, its theoretical basis remains unclear. Nakamura (1989) and Nakamura (2000) argue that the H/V peak frequency is caused by vertically

GJI Seismology

incident *SH* waves yielding a direct estimate of the *S*-wave transfer function and thus any site amplification. Numerical simulations by Lachet & Bard (1994) on the other hand demonstrate that the H/V peak frequency could also be due to the ellipticity of the fundamental Rayleigh wave. The vertical components contain no energy at the observed H/V peak frequency since all Rayleigh waves are then linearly polarized on the horizontal component.

Bonnefoy-Claudet *et al.* (2008) show in a more recent numerical study that the H/V peak frequency is always a good estimate for the theoretical resonance frequency of vertically incident *SH* waves; yet the magnitude of the peak is proportional to the relative portion of Love waves present. This raises the question if Love waves alone could be a cause of the observed resonance frequencies and under what conditions. This question is particularly important since Love waves comprise at least 50 per cent of the noise recordings with local variations of up to 80 per cent (Bonnefoy-Claudet *et al.* 2006b).

Furthermore, resonance frequencies in 1-D media are often analysed using the quarter-wavelength law which is derived for vertically incident *S* waves (Nakamura 2000; Carniel *et al.* 2006). If Love waves could be responsible for the observed resonance frequencies then this raises a second question. Why can the resonance peaks be predicted using the quarter-wavelength law since Love and Rayleigh waves are not composed of vertically incident *S* waves? In addition, the quarter-wavelength law seems to imply that only sources directly underneath the receiver contribute to the recorded resonance frequencies.

I investigate both questions using numerical simulations for a low-velocity layer over a half-space, representing unconsolidated sediments over a bedrock. I analyse the wave motion of *SH* and Love waves only using initially a single source to answer the two questions posed. Results are confirmed by superposing *SH* waves produced by a series of events occurring randomly at various depths, distances and origin times to mimic a natural sequence of microtremors.

First, I describe the modelling and analysis strategy. I then provide an interpretation of the numerical simulations in terms of potential causes for resonance frequencies occurring at all offsets, and finally discuss the wider implications.

2 METHOD

2.1 Quarter-wavelength law

The quarter-wavelength law is frequently employed in site amplification studies to compute the expected resonance frequencies. It is derived based on linear acoustics and checked by a number of measurements for subsurface sediments (Nakamura 2000; Carniel *et al.* 2006).

For standing (body) waves in a single layer over a half-space, the resonance frequency $f_{\text{shear},k}^{\text{vert}}$ for mode k is given by

$$f_{\text{shear},k}^{\text{vert}} = \frac{2k+1}{4}\frac{v_{s,\text{sed}}}{h},\tag{1}$$

where $v_{s,\text{sed}}$ is the *S*-wave velocity in the sediments and h their thickness. The presence of a free surface is crucial. Seismic hazard studies in general assume that the *S*-wave velocity variations within the overburden are small compared with the *S*-wave velocity of the bedrock and can be neglected. Eq. (1) is therefore directly applicable.

2.2 Modelling strategy

The full wavefield is modelled with the reflectivity method (Dietrich 1988). I use a horizontal force in the *y*-direction as a

Table 1. Physical parameters for the simplified sediment–bedrock model.

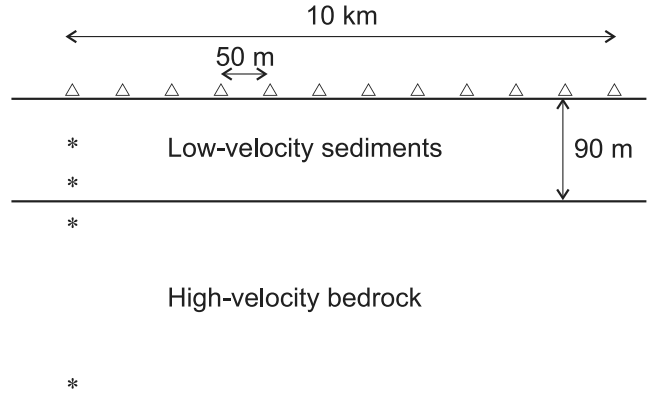| Depth (m)	*S*-wave velocity (m s^{-1})	Density (kg m^{-3})	Q_s
90	250	2000	500
—	1000	2000	500

Figure 1. Source–receiver geometry for the single-source synthetic tests. The triangles sketch the receiver positions buried just underneath the free surface. The stars indicate the relative location of the considered source positions which are always underneath the first receiver. See Table 1 for the physical medium parameters.

point source and analyse the *y*-component of displacement to create *SH* and Love waves only. Site amplification studies assume that unconsolidated sediments exist over a hard bedrock. This is modelled as a low-velocity layer over a half-space. The low-velocity layer has a thickness of 90 m and an *S*-wave velocity $v_{s,\text{sed}} = 250 \text{ m s}^{-1}$. The bedrock is assumed to have an *S*-wave velocity $v_{s,\text{bed}} = 1 \text{ km s}^{-1}$ and infinite thickness. The density and *S*-wave quality factor are kept constant at, respectively, 2.0 g cm^{-3} and 500 everywhere. The *P*-wave velocity is not important since only *SH* and Love waves are considered. Table 1 repeats the model parameters for convenience. The model includes a free surface to generate all multiples and Love waves. The expected resonance frequencies for the first three modes are, respectively, 0.69, 2.08 and 3.47 Hz, eq. (1).

The seismograms are composed of 1024 points, sampled at 65 ms. The seismograms start at −1.04 s to prevent wraparound of a causal arrivals, leading to end times of 65.5 s. This ensures that all relevant arrivals are recorded. The total spread length is 10 km, sampled every 50 m with the first receiver located directly above the source. The receivers are placed just underneath the free surface (Fig. 1). A Ricker wavelet with a peak frequency of 1.5 Hz is used. This value is different from all expected resonance frequencies, yet close enough such that sufficient bandwidth is maintained. See Fig. 2 for the resulting amplitude source spectrum. The source is put at a variety of depths including in and underneath the soft sediments. No geometric spreading corrections are employed but the energy of each trace is normalized for analysis purposes.

2.3 Analysis strategy

In order to understand the simulation results I display the results in a variety of domains, namely (i) the time-offset (*t–x*) domain to show the original synthetics, (ii) the frequency-offset (*f–x*) domain to extract any resonance frequencies as a function of offset, (iii) the intercept time–slowness (*τ–p*) domain to analyse the horizontal
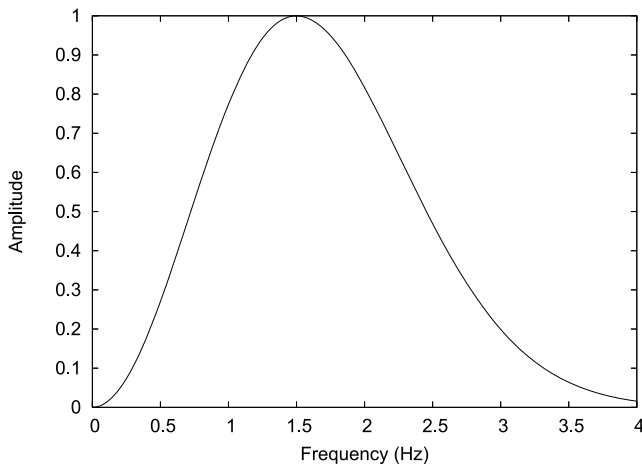
Figure 2. Normalized amplitude spectrum of a Ricker wavelet with a peak frequency of 1.5 Hz.

slownesses present in the synthetics and (iv) the frequency–slowness (f–p) domain to compute the phase–velocity dispersion curves.

The rationale behind this analysis strategy is that the different domains reveal different aspects of the analysed signals. The f–x domain is composed of the amplitude spectrum for each trace. This domain shows how resonance frequencies change with offset for a single source. This is important for assessing whether solely vertical-incidence waves are responsible for any observed resonance frequencies as assumed by the quarter-wavelength law.

The τ–p domain is an intermediate step to obtain the phase–velocity dispersion curves. The τ–p transform maps linear events onto points and hyperbolic moveout curves onto ellipses (Diebold & Stoffa 1981; Van der Baan & Kendall 2002). It also provides pertinent information on the horizontal slownesses of the recorded wavefields due to Snell's law. The latter states that the horizontal slowness is conserved in layered media. Inspection of the τ–p domain wavefields thus reveals the horizontal slownesses at all depths.

The frequency–slowness (f–p) domain is obtained by Fourier transforming the τ–p results to the frequency domain. It displays the phase–velocity dispersion curves of the Love waves in the time-offset synthetics (McMechan & Yedlin 1981) since the horizontal slowness p is the reciprocal of the horizontal phase velocity. Amplitudes in this domain are proportional to the excitation strength of the observed Love-wave dispersion curves. The theoretical phase–velocity dispersion curves are also shown for comparison as computed using Herrmann (2002).

2.4 Snell's law and inhomogeneous waves

Snell's law states that the horizontal slowness p is conserved in laterally homogeneous media. That is,

$$p = \frac{\sin \phi_{\text{sed}}}{v_{s,\text{sed}}} = \frac{\sin \phi_{\text{bed}}}{v_{s,\text{bed}}}, \tag{2}$$

with ϕ_{sed} and ϕ_{bed} the incidence/refraction angle for S-wave ray paths in, respectively, the sediments and the bedrock. The horizontal slowness inside the sediments for the model in Table 1 is thus 4 s km^{-1} and for the bedrock 1 s km^{-1} for horizontal ray paths, and 0 s km^{-1} everywhere for vertical paths.

One could thus conclude that the range of horizontal slownesses for an S-wave source in the sediments is limited between 0 and 4 s km^{-1}, and for a source in the bedrock between 0 and 1 s km^{-1},

given eq. (2) by assuming real-valued angles ϕ_{sed} and ϕ_{bed} between 0° and 90°. Horizontal slownesses larger than 1 s km^{-1} can occur in reality in the bedrock if inhomogeneous waves are recorded.

Inhomogeneous bedrock waves have horizontal slownesses $p > 1/v_{s,\text{bed}}$ or equivalently negative squared vertical slownesses $q_z^2 < 0$ since $v_{s,\text{bed}}^{-2} = p^2 + q_z^2$. Such waves are however rarely recorded in practice since they attenuate exponentially with vertical distance from their point of creation (Stein & Wysession 2003, sections 2.5 and 2.6). Inspection of the recorded wavefields in both the τ–p and f–p domains reveals the observed range of horizontal slownesses and for instance whether or not inhomogeneous waves are present.

An inhomogeneous wave can become a propagating wave again with a real-valued vertical slowness q_z upon entering a low-velocity region. For instance, all inhomogeneous waves in the bedrock with horizontal slownesses in the range 1–4 s km^{-1} impinging upon the bedrock–sediment interface turn into propagating waves inside the sediments with refraction angles between critical incidence and horizontal. This phenomenon is known as wave tunnelling in quantum mechanics (Pain 1983, chapter 12).

3 SIMULATION RESULTS

Fig. 3 displays the t–x seismogram and corresponding f–x spectrum resulting for a source at a depth of 195 m (i.e. inside the bedrock). At first sight it looks like the wavefield is dominated by body wave reverberations with a linear moveout within the top layer. Close inspection reveals however that these linear events are dispersive. Two, possibly three, resonance frequencies are clearly visible at frequencies of 0.65, 2.0 and possibly 3.3 Hz. The quarter-wavelength predictions are reasonable (respectively, 0.69, 2.08 and 3.47 Hz), with a relative error within 5 per cent.

Fig. 4 shows the case for a source inside the sediments at 50 m depth. The t–x section shows a decrease in the contribution of the linear top-layer reverberations. There is also a strong contrast with the previous f–x spectrum (Fig. 3). The resonance frequencies are no longer visible, even though most frequencies are still contained within two bands with a sharp termination at 0.65 Hz. There is also a notch at 2 Hz. Overall the recorded amplitude spectra are similar to the source spectrum (Fig. 2).

Why this remarkable difference between Figs 3 and 4? The principal difference is that the source is in the bedrock in the first case but inside the sediments in the second situation. To illustrate this point, Figs 5 and 6 display the resulting sections for a source at, respectively, 85 and 95 m depth. The sediment–bedrock interface is at 90 m. While the resonance frequencies are starting to become visible in Fig. 5 (source at 85 m), they are significantly sharper in Fig. 6 (source at 95 m)—especially the first resonance frequency is much better defined.

Not all source depths inside the bedrock excite the resonance frequencies equally well. Fig. 7 shows for instance the resulting sections for a source at 500 m depth. The resonance frequencies are significantly less well defined for such a deep source with the first frequency remaining best visible. Simulations for a source at 1000 m depth demonstrate that the resonance frequencies nearly disappear.

4 INTERPRETATION

The reason for the absence, appearance and disappearance again of the resonance frequencies with increasing source depth can be found from analysis of the associated τ–p and f–p sections for a source
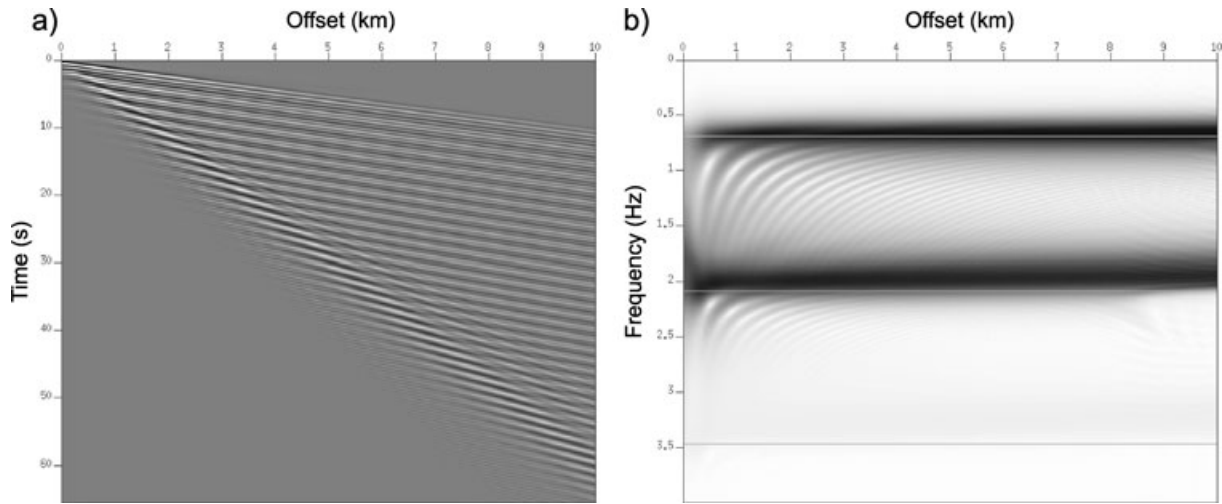
Figure 3. The *t–x* seismogram (a) and *f–x* spectrum (b) for a source at 195 m (inside bedrock). The seismogram is dominated by reverberations in the top layer with a linear but slightly dispersive moveout. There are two, possibly three resonance frequencies visible at 0.65, 2.0 and 3.3 Hz which show little to no offset dependence. Horizontal lines in the *f–x* spectrum represent resonance frequencies predicted by the quarter-wavelength law, eq. (1), which are within 5 per cent of the observed frequencies.
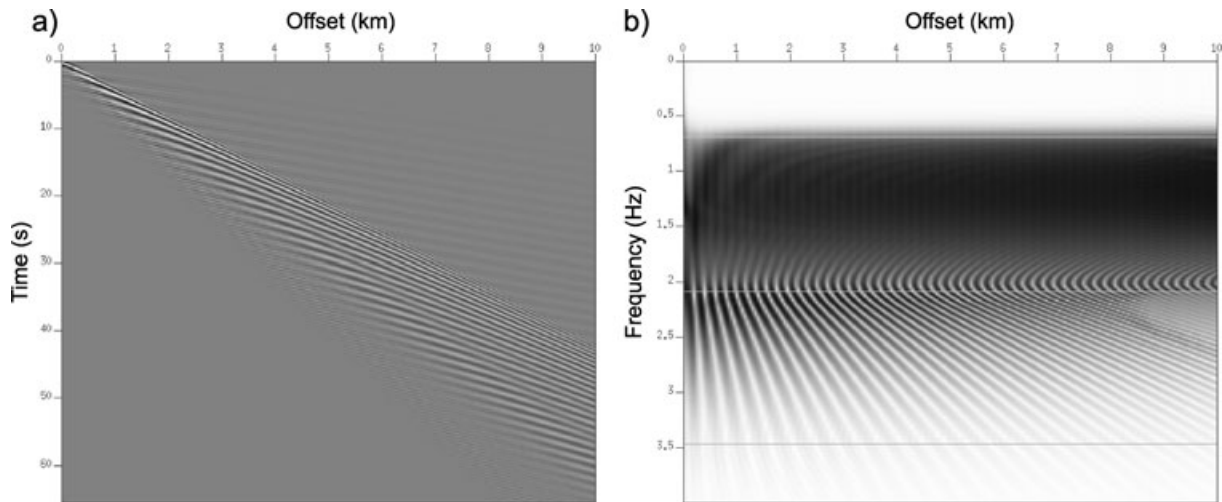

Figure 4. The *t–x* seismogram (a) and *f–x* spectrum (b) for a source at 50 m (inside sediments). The seismogram is now dominated by the Love waves in the top layer, and the resonance frequencies visible in Fig. 3 have been replaced by a continuous spectrum bounded by a notch at 0.65 Hz and possibly 2 Hz and strong interference effects around 2.2 Hz.

at 195 and 50 m, respectively (Figs 8 and 9). Both $\tau-p$ sections are dominated by waves with horizontal slownesses between 1 and 4 s km^{-1} (i.e. the reciprocals of the *S*-wave velocity in, respectively, the bedrock $v_{s,\text{bed}}$ and the soft sediments $v_{s,\text{sed}}$). The *f–p* sections demonstrate that the Love wave dispersion curves are fully excited within the passband of the Ricker wavelet (Fig. 2) for the case of a source in the sediments (Fig. 9). The dispersion curves for the deeper source are on the other hand best excited around the resonance frequencies (Fig. 8).

A horizontally propagating *S* wave in the bedrock has a horizontal slowness of 1 s km^{-1}, whereas the same horizontally propagating wave in the sediments has a horizontal slowness of 4 s km^{-1}, eq. (2). In other words, all horizontal slownesses larger than 1 s km^{-1} for a *S*-wave source in the bedrock (Fig. 8) are associated with inhomogeneous waves which decay exponentially with vertical distance from the source. Once these inhomogeneous waves enter the sediment layer they become propagating waves again if their horizontal slowness is less than 4 s km^{-1} (i.e. $1/v_{s,\text{sed}}$), thereby creating the

observed Love waves. This phenomenon is known as wave tunnelling in quantum mechanics (Pain 1983, chapter 12). The seismograms for the source at 195 m in the bedrock are thus dominated by inhomogeneous *S* waves in the bedrock (Figs 3 and 8). The observed resonance frequencies in the *f–x* spectrum are therefore excited by the inhomogeneous wave components of the bedrock source.

The amplitude *A* of inhomogeneous plane waves in the bedrock as measured at the surface is proportional to

$$A(p, \omega, z_s) \propto \exp[-q_b^{\star}\omega(z_s - h)]\exp[i\omega(px - t)], \qquad (3)$$

where *p* denotes horizontal slowness, ω angular frequency, z_s source depth, *h* the thickness of the sediments and $q_b^{\star}$ the real part of the vertical slowness in the bedrock given by $q_b^{\star} = (p^2 - v_{s,\text{bed}}^{-2})^{1/2}$ with $v_{s,\text{bed}}$ the *S*-wave velocity in the bedrock and $p \geq 1/v_{s,\text{bed}}$ by definition. Expression (3) is derived for inhomogeneous waves propagating along the sediment–bedrock interface. It also provides the amplitude of the tunnelled plane waves at the surface since plane
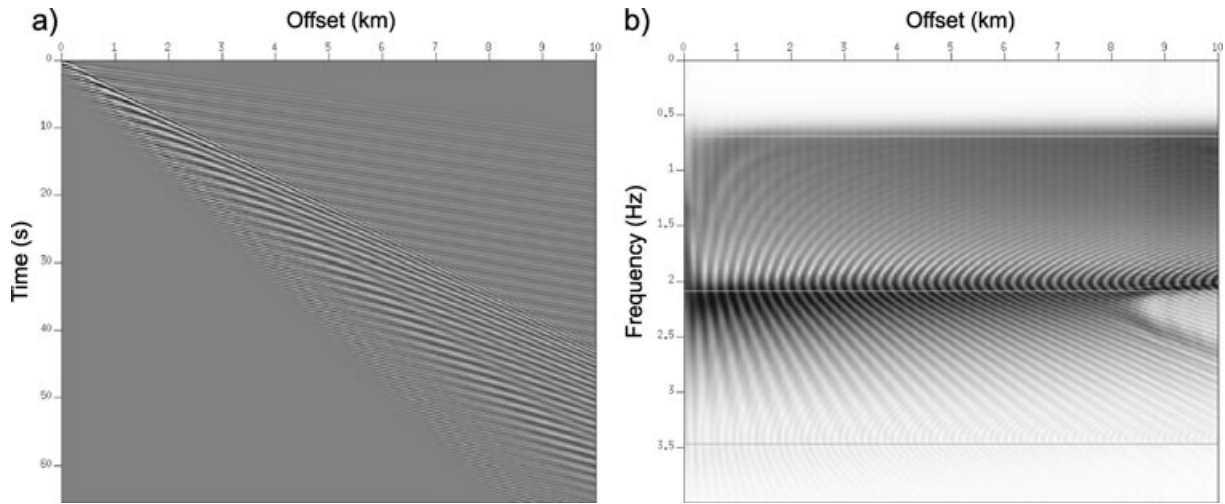
Figure 5. The *t*–*x* seismogram (a) and *f*–*x* spectrum (b) for a source at 85 m (inside sediments). Both linear reverberations and surface waves are visible in the seismogram. The *f*−*x* spectrum does not show the fundamental resonance frequency but the second one is visible although it is affected by interference effects.
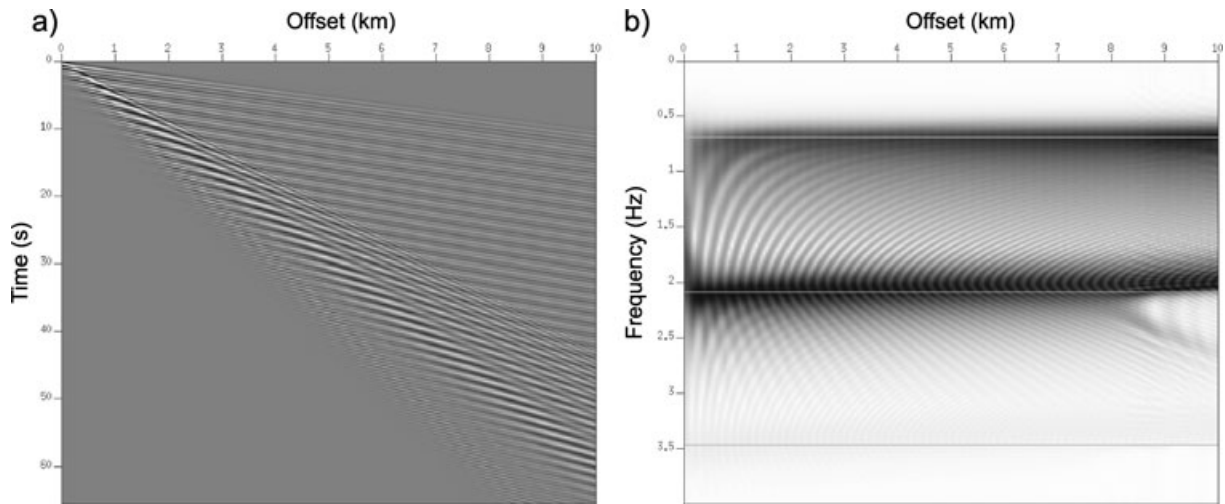

Figure 6. The *t*–*x* seismogram (a) and *f*–*x* spectrum (b) for a source at 95 m (inside bedrock). The *t*–*x* seismogram does not appear to differ significantly from a source at 85 m inside the sediments (Fig. 5a) but the *f*–*x* spectrum clearly shows the existence of two resonance frequencies.
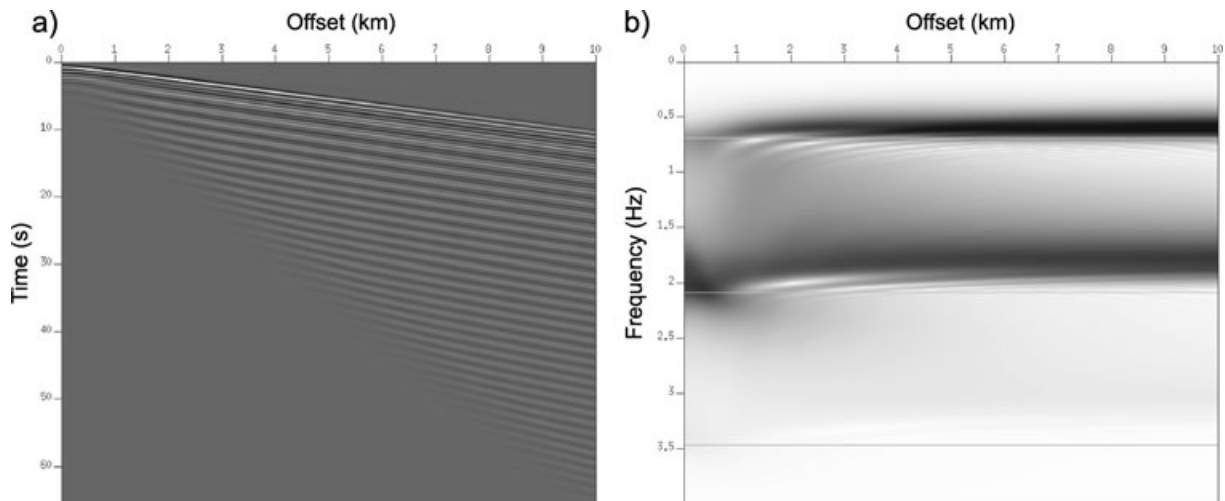

Figure 7. The *t*–*x* seismogram (a) and *f*–*x* spectrum (b) for a source at 500 m (inside bedrock). The seismogram consists entirely of linear reverberations inside the sediments and two resonance frequencies are visible although the second one has a smaller amplitude than for a source at 195 m (Fig. 3). The two resonance frequencies have also shifted to slightly smaller frequencies.
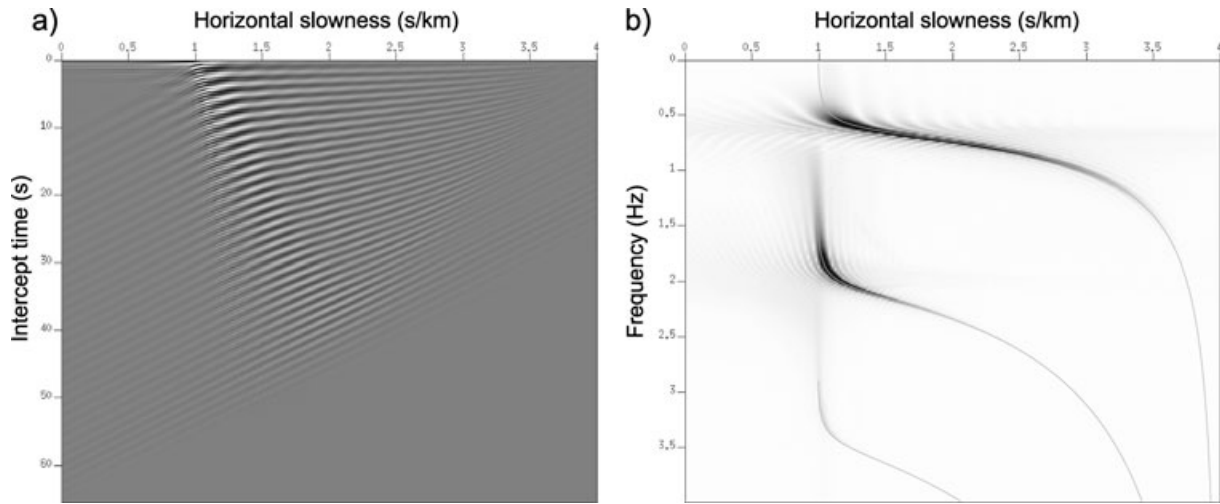
Figure 8. The $\tau-p$ (a) and $f-p$ (b) sections for a source at 195 m. Events in the $\tau-p$ domain are predominantly distributed between horizontal slownesses p of 1 and 3 s km^{-1}, respectively. Both fundamental Love waves and the first higher mode are excited.
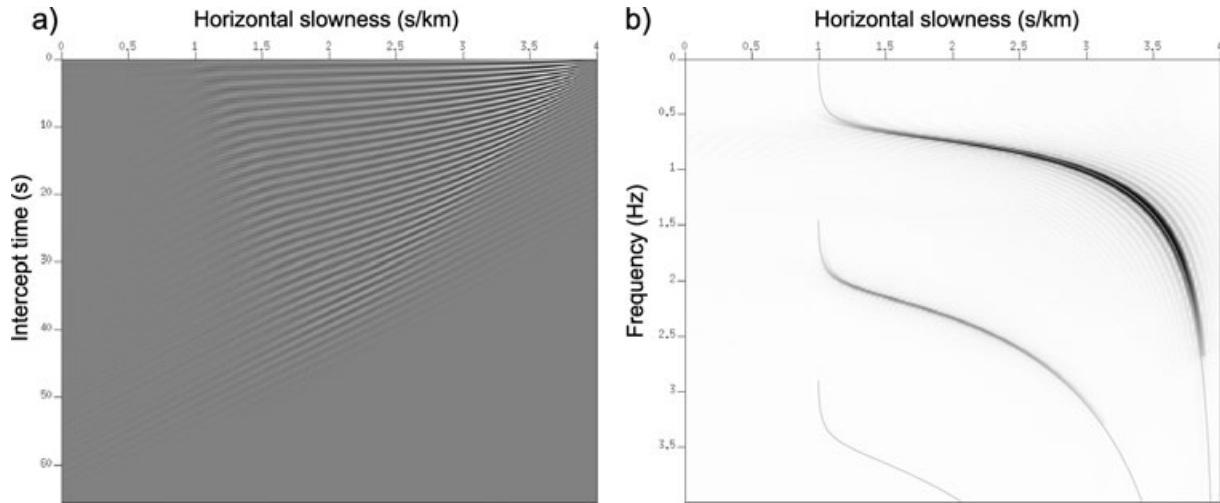

Figure 9. The $\tau-p$ (a) and $f-p$ (b) sections for a source at 50 m. The $\tau-p$ section is now dominated by horizontal slownesses up to the critical slowness of 4 s km^{-1}, and the dispersion curves are likewise excited over a larger slowness range (compare with Fig. 8).

waves in laterally homogeneous media are not subject to geometric spreading (Van der Baan 2004).

Eq. (3) shows that the exponential decay of inhomogeneous waves increases with (i) increasing vertical slowness $q_b^\star$ and thus increasing horizontal slowness p, (ii) increasing source depth $z_s > h$ and (iii) increasing frequency ω. See also fig. 7 in Deng (1994) for an illustration. Eq. (3) explains many features seen in Figs 3–9.

The dispersion curves of the fundamental and first overtone are excited fully for a source in the sediments (Fig. 9) but the maximum excited horizontal slowness is reduced with increasing bedrock source depth ($z_s > h$) because of the exponential amplitude decay of the inhomogeneous S-waves in the bedrock before they materialize into the observed Love waves (Figs 4 and 8). This limits the range of horizontal slownesses impinging on the sedimentary layer from below. Once the inhomogeneous waves enter the sediments they become propagating waves again with a real vertical slowness.

The net result is the creation of plane waves with very specific incidence angles in the sediments that can freely interfere to construct the observed resonance frequencies because all except for a limited range of horizontal slownesses are filtered out by the bedrock. The bedrock thus creates an effective plane-wave source with a reduced range of horizontal slownesses—even though the original source in the bedrock contains all horizontal slownesses (it has an isotropic radiation pattern in the sagittal plane).

The inhomogeneous plane waves are propagating horizontally along the sediment–bedrock interface without amplitude loss since the horizontal slowness p and offset x are only present in the second exponential in eq. (3), that is, in the phase term. This is an additional mechanism that causes the observed resonance frequencies to be independent of offset (Figs 3, 6 and 7).

The inhomogeneous wave amplitudes decay with increasing source depth z_s and increasing frequency ω, eq. (3). Hence a source at 500 m produces less clear resonance frequencies than a source at 195 m, with the lowest frequencies persisting longest (Figs 3 and 7).

In this scenario the observed resonance frequencies are expected to be independent of offset; yet it does not fully explain why the quarter-wavelength law, eq. (1), gives a good prediction of the observed resonance frequencies at all offsets despite its assumption of vertical incidence S waves. Often there is a large contrast in S-wave velocities between the sediments and the bedrock. S waves impinging from below on the sediment–bedrock interface are thus

refracted toward the vertical axis because of the decrease in *S*-wave velocity, eq. (2). This bending to vertical incidence becomes more pronounced for decreasing ratios $v_{s,\text{sed}}/v_{s,\text{bed}} < 1$. The quarter-wavelength law, eq. (1), is exact in the limit $v_{s,\text{sed}}/v_{s,\text{bed}} \rightarrow 0$. It provides an overestimate of the predicted resonance frequencies at all other ratios. This prediction degrades with decreasing contrast between the sediment and bedrock *S*-wave velocity.

The f–p sections (Figs 8 and 9) demonstrate that each observed resonance frequency is directly related to each individual Love wave mode and the precise shape of its dispersion curve. The resonance frequencies are best described by the position of the left knees (i.e. points of maximum curvature) in the phase slowness dispersion curves. The left knees are close to the slowness of horizontally propagating waves in the bedrock (i.e. horizontal propagation in the high-velocity layer and thus critical incidence in the sediments). A slight modification of the quarter-wavelength law can be obtained if we assume that the upgoing waves impinge at this particular slowness, leading to

$$f_{\text{shear},k}^{\text{crit}} = \frac{2k+1}{4}\frac{v_{s,\text{sed}}}{h}\left(1 - \frac{v_{s,\text{sed}}^2}{v_{s,\text{bed}}^2}\right)^{1/2}. \tag{4}$$

Expression (4) lowers the predicted resonance frequencies depending on the ratio $v_{s,\text{sed}}/v_{s,\text{bed}}$ due to the increased ray paths inside the sediments at non-vertical incidence.

For the model in Table 1 this yields for the fundamental mode $f_{\text{shear},0}^{\text{crit}} = 0.67$ Hz which is slightly closer to the observed resonance frequency of 0.65 Hz (Fig. 3) then the original quarter-wavelength prediction $f_{[\text{shear},0}^{\text{vert}} = 0.69$ Hz. Likewise for the first overtone $f_{\text{shear},1}^{\text{crit}} = 2.02$ Hz compared with an observed resonance frequency of 2.0 Hz and $f_{\text{shear},1}^{\text{vert}} = 2.08$ Hz. The difference between both predictions increases with decreasing contrast between the *S*-wave velocities in the sediments and bedrock.

5 ADDITIONAL SIMULATIONS

There are a few additional factors for *SH*-wave resonances in sedimentary layers that are pertinent. What is the influence of the quality factor Q inside the sediments? Is the impedance contrast important? Do the above conclusions uphold for a mixture of sources occurring at random depths, distances and times thus mimicking a natural sequence of microtremors?

5.1 Quality factor

Unconsolidated sediments tend to have significantly lower quality factors than bedrock. Are the resonance frequencies still visible if a more realistic quality factor is considered? Fig. 10 displays the resulting t–x and f–x sections for a quality factor $Q_s = 20$ inside the sediments. All other quantities remain as in Table 1.

The two resonance frequencies remain present despite the more realistic quality factor. The number of reverberations has been reduced in the t–x domain due to the higher attenuation inside the sediments. The resonance frequencies have also shifted to slightly lower values. This is due to the enhanced body wave dispersion because of the reduced quality factor. This shift becomes even more pronounced for lower quality factors.

Constructive interference can already occur after a few multiple reflections within the sediments without the need for long reverberation trains. This permits a low quality factor for a thin sedimentary layer such as in Table 1. The quality factor may play a more important role in very thick sedimentary packages (i.e. thick in comparison with the wavelength of the resonance frequency).

A low quality factor inside the bedrock has a more immediate effect. It attenuates the amount of energy reaching the sediments thereby effectively preventing wave tunnelling but this scenario is geologically implausible.

5.2 Impedance and density contrasts

The impedance contrast influences the resonance frequencies mostly via velocity. Tunnelling only occurs if a wave traverses a high-velocity layer into a low-velocity zone. The sediments must therefore have a lower velocity than the underlying basement. In addition, it is geologically highly plausible that the sediments are characterized by lower densities than the basement, leading to positive impedance contrasts.

Density has only a very moderate influence on the Love-wave dispersion curves (Gupta & Grant 1963). Considerable density changes are thus required before noticeable shifts in resonance frequencies occur. On the other hand, density is likely to have a much stronger influence on site amplification (Boore & Joyner 1997).

Fig. 11 contains the $t-x$, $f-x$ and $f-p$ sections for a considerably reduced velocity contrast. The sedimentary *S*-wave velocity has
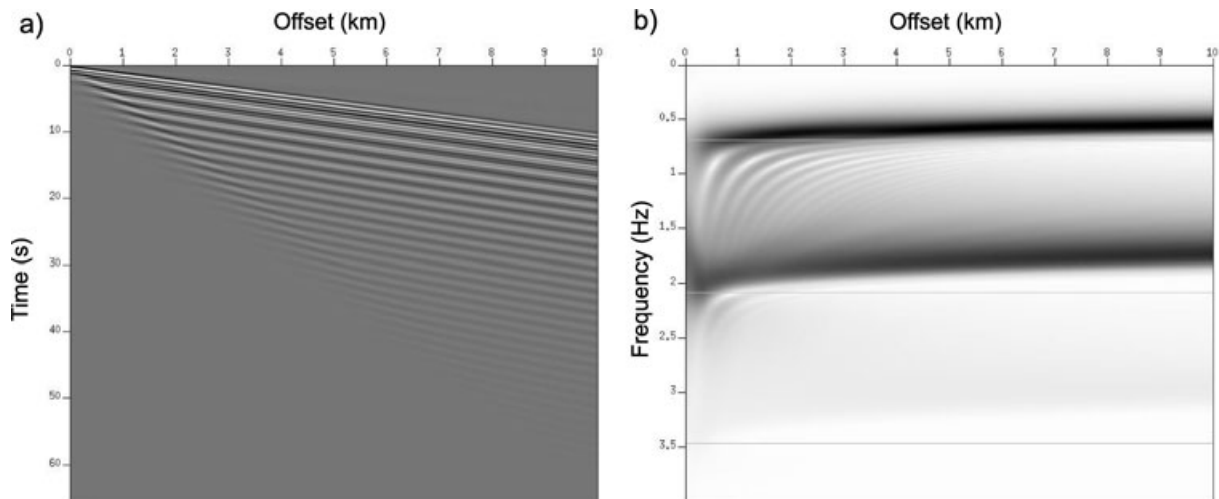

Figure 10. The t–x (a) and f–x (b) sections for a source at 195 m but with a realistic quality factor $Q_s = 20$ in the sediments. Compare with Fig. 3. Both resonance frequencies remain visible although slightly shifted.
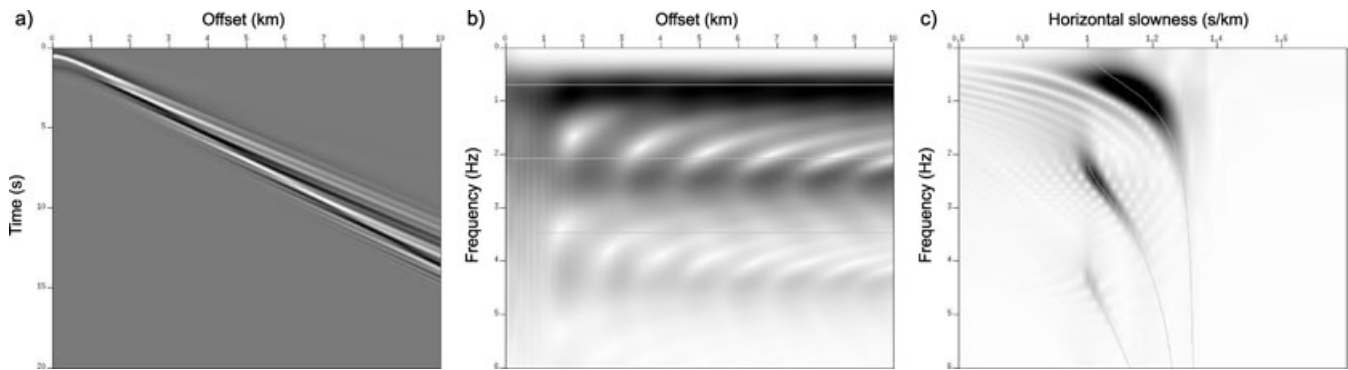
Figure 11. The *t–x* (a), *f–x* (b) and *f–p* (c) sections for a source at 395 m and a tripled sedimentary *S*-wave velocity and thickness. Compare with Fig. 3. The lower velocity contrast has considerably shifted the position of the resonance frequencies. Only the modified quarter-wave length law, eq. (4), can handle such a low velocity contrast.

been increased to $v_{s,\text{sed}} = 0.75\,\text{km s}^{-1}$. The sediment thickness has been tripled to 270 m as well to maintain the resonance frequencies predicted by the vertical quarter-wavelength law, eq. (1). All other physical parameters are as in Table 1. Simulations using three Ricker wavelets with peak frequencies of, respectively, 0.75, 1.5 and 3 Hz are summed in order to enlarge the excited frequency range.

The *t–x* seismogram is very different from the previous Figs 3–10. Not only is the signal duration much shorter (note different vertical timescale) but there are also more complex and highly dispersive interference patterns (Fig. 11a). The resonance frequencies in the *f–x* section (Fig. 11b) are therefore less well excited and display more variability than for the high-contrast case (e.g. Fig. 3b). The resonance frequencies correspond again to the left-most kinks in the phase–velocity dispersion curves (Fig. 11c). This is also true for the fundamental frequency. It appears in this simulation as excited at a larger frequency due to the lack of sufficiently low-frequency content in the employed source wavelets.

The vertical quarter-wavelength law, eq. (1), does not take the bedrock *S*-wave velocity into account, and its predictions are inaccurate for such a low velocity contrast (grey lines in Fig. 11b). The modified law, eq. (4), yields resonance frequencies of, respectively, 0.46, 2.30 and 4.13 Hz which are very close to the observed ones. It also predicts resonance frequencies at 1.38 and 3.22 Hz which are non-existent. These intermediate resonance frequencies are still present for larger contrasts up to $v_{s,\text{sed}} = 0.5\,\text{km s}^{-1}$ (with fixed $v_{s,\text{bed}} = 1\,\text{km s}^{-1}$) but the corresponding Love-wave dispersion branches disappear for lower velocity contrasts.

Note also that the resonance frequencies are not only more prone to interference but also spread out over a larger frequency range. This is probably due the less pronounced kinks in the dispersion curves with smaller concentrations of areas with high curvature (Fig. 11c).

Resonance frequencies occur thus even for low velocity contrasts. The modified quarter-wavelength law, eq. (4), is more accurate than the original version, eq. (1), with the exception of the disappearing resonance frequencies for small velocity contrasts.

5.3 Random, multiple sources

The single-source simulations mimic site-amplification studies where seismic recordings of an earthquake over unconsolidated sediments and a local bedrock outcrop are compared by means of a spectral division (Dutta *et al.* 2001). A proper comparison

with site-reference studies would divide all previous *f–x* plots with the frequency spectrum of a Ricker wavelet (Fig. 2) since a local bedrock outcrop corresponds in the above simulations to a homogeneous half-space where only the direct *SH* wave is recorded. This spectral division was not deemed necessary since any resonance frequencies are very sharp when present. The above conclusions are therefore appropriate for *SH*-wave resonances due to a single earthquake.

Is wave tunnelling also responsible for resonance frequencies in microseismic noise? It is a common assumption that microseismic noise can be simulated as seismic events occurring at random times, depths and epicenters (Field & Jacob 1993; Lachet & Bard 1994; Bonnefoy-Claudet *et al.* 2006a, 2008). Several realizations of random events were created for the model in Table 1.

The source depths have a uniform distribution within the sediments and decay exponentially in the bedrock to mimic the fact that microseismic noise is likely to be dominated by human-induced activity close to the surface (Bonnefoy-Claudet *et al.* 2006b). Fig. 12(a) displays the source distribution. On the other hand brittle failure is more likely in the bedrock than the unconsolidated sediments. The average amplitude of bedrock sources is chosen to be one order of magnitude larger than those in the sediments.

Origin times, source distances and amplitude scaling factors are all modelled using Gaussian distributions with standard deviations of, respectively, 30 s, 1 km and a value of 100. The average epicentre is placed 5 km away from the single receiver to simulate a distant noise source and reduce the effect of the highly energetic direct wave for an event immediately underneath the receiver (Fig. 13). Both the origin time and scalar magnitude have zero-mean distributions. Five random events occur at each depth but with different origin times, epicentral distances and magnitudes.

Fig. 12(b) shows the resulting frequency spectra of random *SH* sources occurring, respectively, only in the sediments (dashes) or bedrock (dots), as well as the source spectrum for reference (Fig. 2). It demonstrates that only sources in the bedrock create unmistakably sharp resonance frequencies. The two resonance frequencies for bedrock sources remain visible for different realizations of the noisefield whereas the resulting spectra for sedimentary sources are much more variable. The amplitude of the resonance frequencies above the background spectrum depends thus on the relative location and strength of the sources creating the microseismic noise. This could provide pertinent geologic information on the causes and origin of the microseismic noisefield but it also complicates site-amplification studies.
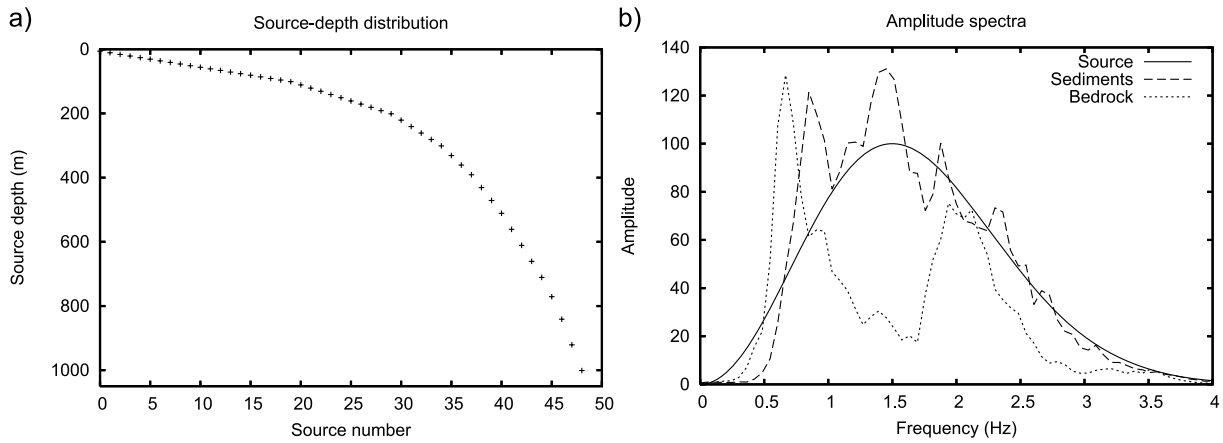
Figure 12. Microseismic noise simulated by randomly occurring events. (a) Source-depth distribution of the random events. The number of events decreases with depth to emphasize surface-related microseismicity. (b) The resulting frequency spectra for sources only in the bedrock (dots, $z_s > 90$ m) or sediments (dashes, $z_s < 90$ m). The source wavelet is shown for reference as well. Sources in the bedrock are needed to excite the resonance frequencies indicating that wave tunnelling is the dominant cause of *SH*-wave resonances in both single earthquakes and microseismic noise.
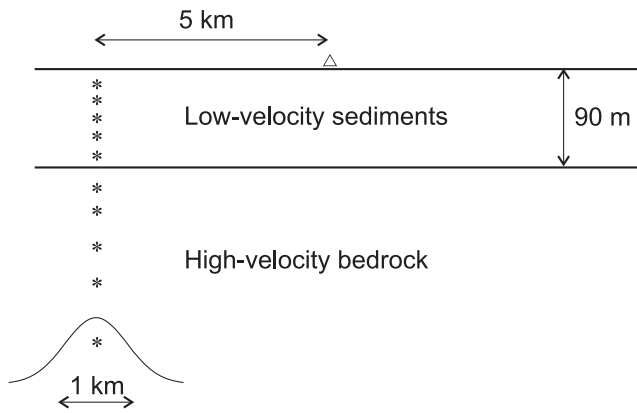

Figure 13. Sketch of source–receiver geometry for multisource simulation. A single receiver (triangle) records a variety of randomly occurring events (stars) located on average 5 km away. See Table 1 for the physical medium parameters.

6 DISCUSSION AND WIDER IMPLICATIONS

Analysis of ambient noise has shown that Love waves represent at least 50 per cent of the recorded wavefields with local variations up to 80 per cent (Bonnefoy-Claudet *et al.* 2006b). Bonnefoy-Claudet *et al.* (2008) demonstrate in a recent numerical study that the magnitude of the H/V peak is proportional to the relative portion of Love waves present. Nakamura (1989, 2000) argues that computing the spectral ratio of H/V ground motion neutralizes the effect of any Rayleigh waves and that any observed spectral peaks are caused by vertically incident *SH* waves. Inspection of H/V spectra produces then a direct estimate of the *S*-wave transfer function, thus providing an accurate estimate of any site amplification.

The current study looks at horizontal spectra only and cannot reveal if computing the spectral ratio H/V de-emphasizes any Rayleigh waves. It does not examine in detail the precise strength of the observed resonance frequencies or their relation to site amplification factors for seismic risk studies. However, it demonstrates that *SH* sources in the bedrock lead to sharp resonance frequencies at almost

all offsets (Figs 3, 6 and 7). Love and Rayleigh waves are decoupled in laterally homogeneous media. This phenomenon is thus independent of the Rayleigh wave polarization which has a supplementary effect on any observed resonance frequencies and site-amplification factors.

The position of the resonance frequencies relate directly to the shape of the Love-wave dispersion curves (Fig. 8). The H/V peak frequency provides thus an initial estimate of the ratio $h/v_{s,\text{sed}}$ if it is caused predominantly by Love waves in a soft sedimentary layer, as argued by Nakamura (1989, 2000). Empirically it has been shown that the peak H/V frequency is close to the theoretical resonance frequency for vertically incident *SH* waves if a large impedance contrast exists between the sediments and the bedrock. The Nakamura technique has therefore been the basis for many site investigations (Field & Jacob 1993, 1995; Lermo & Chávez-García 1994; Bonnefoy-Claudet *et al.* 2006b). Furthermore, applying array analysis techniques on the noise recordings reveals the surface wave dispersion curves which can subsequently be inverted for a more detailed velocity profile. This is for instance the basis of the microtremor survey technique (Okada 2003).

How likely is it that inhomogeneous *SH*-source components in the bedrock are the only contributing factor to observed resonance frequencies on horizontal components or H/V peak frequencies? No undisputable resonance frequencies are created for a single *SH* source unless the source is in the bedrock or possibly very close to the sediment bottom (Figs 4–6). This is confirmed by a multisource simulation (Fig. 12b). Ambient noise recordings are characterized by a day-and-night cycle with the largest magnitude occurring during day time (Bonnefoy-Claudet *et al.* 2006b). This points to human activity as the major source for ambient noise which is by its nature predominantly positioned at the Earth's surface. The contribution of bedrock sources to the total recorded noise field can thus be considered to be minor. The fact that the observed resonances are caused by inhomogeneous waves that decay exponentially with increasing vertical separation between the source depth z_s and sediment bottom h, eq. (3), limits their contribution even further.

On the other hand, simulations by Bonnefoy-Claudet *et al.* (2008) demonstrate that the strength of the H/V peak frequency is proportional to the relative portion of Love waves present. This could indicate that computing the H/V spectral ratio indeed de-emphasizes any

Rayleigh wave contributions and that inhomogeneous *SH*-source components in the bedrock play a major role in the creation of the observed resonance frequencies.

It is therefore unlikely that deep *SH* sources are the only cause of observed resonance frequencies on horizontal components or in H/V spectral ratios; yet they can have a strong contribution. This confirms 1-D simulations by Bonnefoy-Claudet *et al.* (2006a) who also observe clear resonance frequencies for sources under the sediments. This paper provides an explanation for this observation.

7 CONCLUSIONS

SH-wave resonances in 1-D sedimentary layers are related to the presence of low-velocity waveguides. The resonance frequencies are created by constructive interference of *SH* waves with a limited range of very specific incidence angles in the sedimentary layer. One general trigger mechanism for this is by inhomogeneous waves tunnelling through the bedrock into the sediments. This permits for a bedrock source with an angle-independent radiation pattern but simultaneously leads to a restricted range of incidence angles within the sediments. Sharp resonances are then visible at almost all epicentral distances.

The resulting *SH*-wave resonances correspond to points of maximum curvature in the Love-wave phase–velocity dispersion curves. They are formally still surface waves although they appear in the time-offset domain as linear but slightly dispersive events. This indicates that Love waves alone can be responsible for any observed peak frequencies in the spectral ratios of H/V ground motion, in particular if computation of this ratio de-emphasizes any Rayleigh wave contributions. However, other mechanisms cannot be ruled out.

The inhomogeneous waves decay exponentially with increasing horizontal slowness, increasing depth below the sediments and increasing frequency. The fundamental frequency tends thus to have the largest contribution to the observed wave field with horizontal slownesses at or just beyond the critical slowness in the sedimentary layer. The quarter-wavelength law assumes that resonance frequencies are caused by vertically incident *S* waves. This is a reasonable assumption for large velocity contrasts between sediments and bedrock since the critical angle is then close to zero. More accurate predictions are obtained by assuming that *SH*-wave resonances occur at the critical angle.

The multisource simulations show also that site amplification factors as determined by H/V spectral ratios would not only depend on the relative portion of Love waves in the total wavefield (Bonnefoy-Claudet *et al.* 2008) but also on the depth distribution and the relative strength of the *SH* sources inside the bedrock compared with those in the sediments. An accurate interpretation of site amplification factor by means of H/V peak frequencies would thus require in-depth knowledge of the causes and origins of the local microseismic noise field.

ACKNOWLEDGMENTS

REFERENCES

Bonnefoy-Claudet, S., Cornou, C., Bard, P.-Y., Cotton, F., Moczo, P., Kristek, J. & Fäh, D., 2006a. H/V ratio: a tool for site effects evaluation. Results from 1-D noise simulations, *Geophys. J. Int.,* **167,** 827–837.

Bonnefoy-Claudet, S., Cotton, F. & Bard, P.-Y., 2006b, The nature of noise wavefield and its applications for site effects studies: a literature review, *Earth-Sci. Rev.,* **79,** 205–227.

Bonnefoy-Claudet, S., Köhler, A., Cornou, C., Wathelet, M. & Bard, P.-Y., 2008. Effects of Love waves on microtremor H/V ratio, *Bull. seism. Soc. Am.,* **98,** 288–300.

Boore, D.M. & Joyner, W.M., 1997. Site amplification for generic rock sites, *Bull. seism. Soc. Am.,* **87,** 327–341.

Borcherdt, R.D., 1970. Effects of local geology on ground motion near San Francisco Bay, *Bull. seism. Soc. Am.,* **60,** 29–61.

Carniel, R., Barazza, F. & Pascolo, P., 2006. Improvement of Nakamura technique by singular spectrum analysis, *Soil Dyn. Earthq. Eng.,* **26,** 55–63.

Deng, H.L., 1994. Acoustic-wave propagation in thin-layered media with steep reflectors, *Geophysics,* **59,** 1593–1604.

Diebold, J.B. & Stoffa, P.L., 1981. The traveltime equation, tau-*p* mapping, and inversion of common midpoint data, *Geophysics,* **46,** 238–254.

Dietrich, M., 1988. Modeling of marine seismic profiles in the *t*−*x* and *τ*−*p* domains, *Geophysics,* **53,** 453–465.

Dutta, U., Martirosyan, A., Biswas, N., A, A.P. & Combellick, R., 2001. Estimation of S-wave site response in Anchorage, Alaska, from weak-motion data using generalized inversion method, *Bull. seism. Soc. Am.,* **91,** 335–346.

Field, E.H. & Jacob, K.H., 1993. The theoretical response of sedimentary layers to ambient seismic noise, *Geophys. Res. Lett.,* **20,** 2925–2928.

Field, E.H. & Jacob, K.H., 1995. A comparison and test of various site-response estimation techniques, including three that are not reference-site dependent, *Bull. seism. Soc. Am.,* **85,** 1127–1143.

Gupta, R.N. & Grant, F.S., 1963. Theoretical love wave dispersion in a single layer model, *Pure appl. Geophys.,* **55,** 16–20.

Herrmann, R.B., 2002. *Computer Programs in Seismology, Version 3.30,* Saint Louis University, USA.

Lachet, C. & Bard, P.-Y., 1994. Numerical and theoretical investigations of the possibilities and limitations of Nakamura's technique, *J. Phys. Earth,* **42,** 377–397.

Lermo, J. & Chávez-García, F.J., 1994. Are microtremors useful in site response evaluation?, *Bull. seism. Soc. Am.,* **84,** 1350–1364.

McMechan, G.A. & Yedlin, M.J., 1981. Analysis of dispersive waves by wave field transformation, *Geophysics,* **46,** 869–874.

Nakamura, Y., 1989. A method for dynamic characteristics estimation of subsurface using microtremor on the ground surface, *Quart. Report Railway Tech. Res. Instit. Japan,* **30**(1), 25–33.

Nakamura, Y., 2000. Clear identification of fundamental idea of Nakamura's technique and its applications, *Proceedings of the XII World Conf. Earthquake Engineering,* New Zealand, p. Paper no. 2656.

Nogoshi, M. & Igarashi, T., 1971. On the amplitude characteristics of microtremor (part 2), *J. Seism. Soc. Japan,* **24,** 26–40.

Okada, H., 2003. *The Microtremor Survey Method,* Society of Exploration Geophysicists.

Pain, H.J., 1983. *The Physics of Vibrations and Waves,* 3rd edn, Wiley, Chichester.

Stein, S. & Wysession, M., 2003. *An Introduction to Seismology, Earthquakes and Earth Structure,* Blackwell Publishing, Oxford.

Van der Baan, M., 2004. Processing of anisotropic data in the *τ*−*p* domain: I—geometric spreading and moveout corrections, *Geophysics,* **69,** 719–730.

Van der Baan, M. & Kendall, J.-M., 2002. Estimating anisotropy parameters and traveltimes in the *τ*−*p* domain, *Geophysics,* **67,** 1076–1086.